Graefe's Archive for Clinical and Experimental Ophthalmology (2021) 259:2225–2234
https://doi.org/10.1007/s00417-021-05105-3

RETINAL DISORDERS

Development of a deep-learning system for detection of lattice degeneration, retinal breaks, and retinal detachment in tessellated eyes using ultra-wide-field fundus images: a pilot study

Chenxi Zhang[1] · Feng He[1] · Bing Li[1] · Hao Wang[2] · Xixi He[2] · Xirong Li[3,4] · Weihong Yu[1] · Youxin Chen[1]

Received: 24 October 2020 / Revised: 10 January 2021 / Accepted: 26 January 2021 / Published online: 4 February 2021

Abstract

Purpose To investigate the detection of lattice degeneration, retinal breaks, and retinal detachment in tessellated eyes using ultra-wide-field fundus imaging system (Optos) with convolutional neural network technology.

Methods This study included 1500 Optos color images for tessellated fundus confirmation and peripheral retinal lesion (lattice degeneration, retinal breaks, and retinal detachment) assessment. Three retinal specialists evaluated all images and proposed the reference standard when an agreement was achieved. Then, 722 images were used to train and verify a combined deep-learning system of 3 optimal binary classification models trained using seResNext50 algorithm with 2 preprocessing methods (original resizing and cropping), and a test set of 189 images were applied to verify the performance compared to the reference standard.

Results With optimal preprocessing approach (original resizing method for lattice degeneration and retinal detachment, cropping method for retinal breaks), the combined deep-learning system exhibited an area under curve of 0.888, 0.953, and 1.000 for detection of lattice degeneration, retinal breaks, and retinal detachment respectively in tessellated eyes. The referral accuracy of this system was 79.8% compared to the reference standard.

Conclusion A deep-learning system is feasible to detect lattice degeneration, retinal breaks, and retinal detachment in tessellated eyes using ultra-wide-field images. And this system may be considered for screening and telemedicine.

Keywords Deep learning · Lattice degeneration · Retinal breaks · Retinal detachment · Tessellated fundus · Ultra-wide-field fundus imaging

Chenxi Zhang, Feng He and Bing Li contributed equally to this work.

This article is part of a topical collection on *Breakthroughs in artificial intelligence for ophthalmology.*

✉ Weihong Yu
yuwh@pumch.cn

✉ Youxin Chen
chenyx@pumch.cn

[1] Department of Ophthalmology, Key Laboratory of Ocular Fundus Diseases, Peking Union Medical College Hospital, Chinese Academy of Medical Sciences and Peking Union Medical College, 1# Shuai Fu Yuan, Dongcheng District, Beijing 100730, China

[2] Vistel AI Lab, Visionary Intelligence Ltd, Beijing, China

[3] Key Lab of Data Engineering and Knowledge Engineering, Renmin University of China, Beijing, China

[4] AI & Media Computing Lab, School of Information, Renmin University of China, Beijing, China

Key Messages

- Deep learning models based on ultra-wide-field (Optos) images to identify retinal detachment or notable peripheral retinal lesions have been developed and showed high accuracy in different studies.
- In the study, we developed an Optos-based deep learning system that combined the detection of retinal detachment with its predisposing peripheral lesions, lattice degeneration and retinal breaks in tessellated eyes and classified lattice degeneration and retinal breaks independently.
- The feasibility of our deep learning system was verified withan area under curve of 0.888, 0.953 and 1.000 for detection of lattice degeneration, retinal breaks and retinal detachment respectively and a referral accuracy of 79.8% compared to the reference standard.
- Our system may be utilized for screening and telemedicine applications.

Introduction

A significant increase in prevalence of high myopia has been noted in recent decades. It is estimated that nearly 1 billion people, 10% of the world, will have high myopia by 2050 [1]. Such trend has also been observed in myopic-related complications, which can cause irreversible vision loss. Retinal detachment, as one of the complications, can lead to blindness without prompt intervention. Higher incidence of retinal detachment is associated with the increased axial lengths of highly myopic eyes, so do the predisposing features of retinal detachment, lattice degeneration, and retinal breaks [2–4]. The prevalence of the former increases from approximate 8% of the general population to 17% of high myopic patients and the latter occurs 8% of high myopes [3, 5].

Tessellated fundus, defined as increased visibility of the underlying choroidal vessels around the fovea and arcade vessels, is often regarded as the commencement of retinochoroidal degenerative changes in high myopia [6]. And nearly 50% of tessellated eyes of high myopic patients presented with peripheral retinal degeneration [7]. Therefore, it is essential to access the peripheral retina in tessellated eyes for early detection of retinal detachment and close monitoring of its related predisposing conditions, lattice degeneration, and retinal breaks. However, a thorough examination of peripheral retina requires professional vitreoretinal skills of the ophthalmologists and pupil dilation of the patients, which is not feasible for routine considering retinal specialist shortage, increased risk of pupillary block, and blurred vision after mydriasis in clinical practice.

Thanks to the advances of retinal imaging in recent years, with the introduction of Optos, an ultra-wide-field scanning laser ophthalmoscope, up to 200° of retina (covering 80% of the fundus) can be captured in a single shot noninvasively, even under non-mydriasis, providing a high efficient modality for peripheral retina screening while avoiding the risk of pupillary block and minimizing inconvenience caused by mydriasis [8, 9]. The device has been widely utilized in the diagnosis or follow-up of various fundus diseases, and the simple operation procedure makes it possible for telemedicine use in underserved areas [9, 10].

Deep-learning algorithms have been successfully applied to ophthalmology in recent years, and deep-learning models based on Optos images, utilizing its advantage of peripheral retina imaging, have also been developed and showed high accuracy in identifying retinal detachment or notable peripheral retinal lesions in different studies [10–14]. However, so far, there have been no deep-learning models based on Optos images that are able to detect retinal detachment and its predisposing peripheral lesions, lattice degeneration, and retinal break simultaneously in one screening system, and previous study on notable peripheral retinal lesions did not classify lattice degeneration and retinal breaks independently.

In this study, we aimed to develop and assess a deep-learning system for detecting lattice degeneration, retinal breaks, and retinal detachment independently in tessellated fundus using Optos images.

Methods

This study was approved by the Institutional Review Board of Peking Union Medical College Hospital, China and conducted in compliance with the Declaration of Helsinki.

Datasets

For dataset establishment, initial 1500 consecutive Optos (Daytona, Optos PLC, Dunfermline, UK) color images were retrospectively obtained from patients presenting for fundus evaluation between August, 2017 and December, 2018 at Beijing Hua'er Eye Hospital. All images were checked for

duplicate acquisition and deidentified before further assessment.

Firstly, all these images were reviewed by 2 retinal specialists independently to confirm the presence of tessellated fundus. Only those with consensus agreement were registered as tessellated dataset. Secondly, since we aimed to screen for lattice degeneration, retinal breaks, and retinal detachment in untreated tessellated fundus, we excluded poor-quality images that were not feasible for tessellation discrimination or with ≥25% peripheral region was obscured. Unclear images attributed to vitreous hemorrhage, astrocytosis, or intense cataracts and images showing signs of previous vitreoretinal surgery or retinal photocoagulation were also excluded at this step.

The features of lattice degeneration, retinal breaks, and retinal detachment were characterized and described in Table 1, according to the Posterior Vitreous Detachment, Retinal Breaks, and Lattice Degeneration Preferred Practice Pattern® (PPP) guidelines [15]. Investigators identified the three target findings (lattice degeneration, retinal breaks, and retinal detachment) and annotated their corresponding lesion location in images from tessellated dataset. Images with other peripheral retinal lesions rather than the target ones, such as hemorrhage, hard exudate, or cotton-wool patch, were excluded at the annotation step.

To ensure an accurate identification of target lesions, all anonymous images were assessed independently by 3 retinal specialists. A consensus identification outcome was given to an image only when agreement was achieved among the 3 retinal specialists. Any level of inconsistency brought a discussion among 3 assessors, and images unable to achieve a consensus in final discussion were discarded. The consensus identification outcome served as the reference standard for deep-learning system development. Figure 1 illustrates the workflow of image processing.

Of all eligible tessellated images, 60% were used for training, while 20% for validation of the trained model and 20% for performance assessment.

Development of deep-learning system

Our screening system contains 3 binary classification models to detect lattice degeneration, retinal breaks, and retinal detachment. We analyzed the outputs of the 3 models comprehensively to get the final prediction.

Convolutional neural network architecture

The state-of-the-art convolutional neural network (CNN) architecture seResNext50 was used for training the binary classification models [16]. The CNN seResNext50 is based on ResNext50 with the SE module applied in each ResNext block [17]. The SE module learns the correlation between feature maps of different channels and applies a larger weight factor to the more effective feature maps. We used the weights pretrained on the ImageNet dataset to initialize the CNN.

Image preprocessing

We investigated two image preprocessing methods:

(1) Original resizing method: Original images were resized to 512 × 512 for training, validation, and test set. The

Table 1 Images categories and their corresponding clinical features

Classification	Presence of clinical features
Tessellated	Well-defined choroidal vessels can be observed clearly around the fovea and arcade vessels.
Treated	Presence of any sign of previous vitreoretinal surgery or retinal photocoagulation
Untreated	No sign of previous vitreoretinal surgery or retinal photocoagulation
Lattice degeneration	Peripheral circumferentially oriented linear or ovoid retinal thinning with/without whitish lines, reddish crater-like appearance, superficial whitish yellow flecks, and pigmentary disturbances
Retinal breaks	Full-thickness defects in the retina including round atrophic holes and horseshoe-shaped tears due to vitreoretinal traction
Retinal detachment	A separation of the retina from the retinal pigment epithelium
Other peripheral retinal lesions	Any peripheral retinal abnormality rather than the 3 target lesions above
No significant peripheral retinal lesions	None of the above peripheral manifestations
Non-tessellated	No presence of tessellation changes
Poor quality	Insufficient for tessellation discrimination or peripheral evaluation (≥25% of the peripheral region was obscured, vitreous hemorrhage, astrocytosis, or intense cataracts)

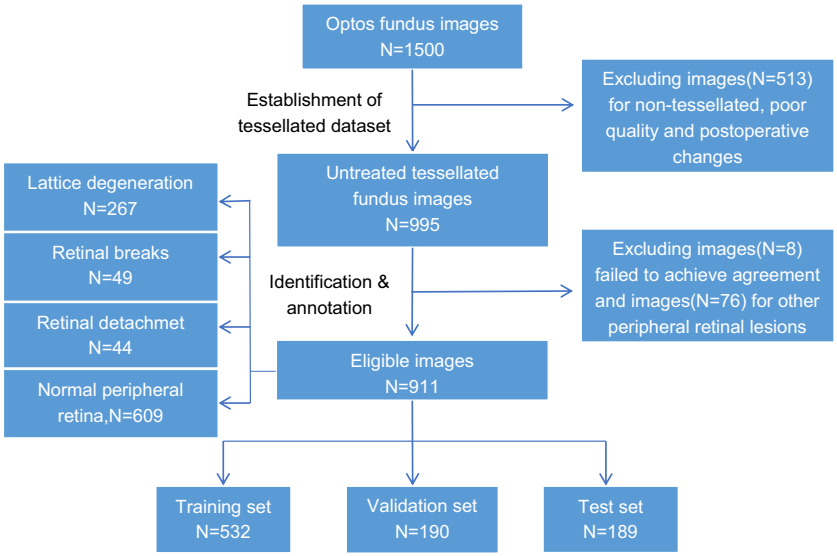

Fig. 1 The workflow of establishing Optos image datasets for deep-learning system development

model took the whole image as the input and output of a positive score for each lesion per image.

(2) Cropping method: For training set, if an image was with no abnormality, negative patches were cropped from the raw image (resolution about 2000 to 3000) with size randomly selected from {448 × 448, 512 × 512, 640 × 640, 720 × 720} using sliding window. The stride of the sliding window was set to half of the window size. If an image was annotated with lesions, 20 positive patches were selected for each lesion blob. For each lesion blob, 5 different positions of patch center were randomly selected around the center of the lesion blob and 4 different patch sizes ({448 × 448, 512 × 512, 640 × 640, 720 × 720} for retinal breaks, {512 × 512, 640 × 640, 720 × 720, 896 × 896} for lattice degeneration, and {640 × 640, 720 × 720, 896 × 896, 1024 × 1024} for retinal detachment) were selected for each position. All the selected patches were finally resized to 512 × 512. The model took a patch as the input and output of a positive score for each lesion per patch. For test set and validation set, a sliding window with size 512 × 512 and stride 256 × 256 was adopted to the raw image. The positive score of a lesion of an image was taken as the max score of all the image's patches.

Model implementations

The SGD optimizer was applied to train the models with momentum of 0.9 and weight decay of 0.0001. The learning rate for epochs 1-5 was 0.01 and was 0.005 for epochs 6-15. After epoch 15, the learning rate would be halved if the performance on validation set did not increase for two consecutive epochs. The batch size was set to 10.

Data augmentation was adopted during training. Random rotation, horizontal and vertical flipping, random crop, brightness shift, contrast transform, and saturation transform were applied.

Heatmap

To locate the most focused region of deep-learning system and check the reasons for misclassified images, heatmaps were generated using Class Activation Mapping (CAM) technology for all true-positive and false-positive images [18]. CAM visualizes the images in which the most salient pixels for models' prediction are highlighted.

Statistical analysis

We examined the areas under receiver operating characteristic curve (AUCs) with 95% confidence intervals to evaluate the performance of each deep-learning model; sensitivity and specificity that yielded the highest harmonic mean with the 95% confidence intervals were also applied to assess deep-learning models.

Our screening system consists of the better deep-learning model for each finding. Referral accuracy of our screening system was calculated compared to the reference standard. Eligible images with any of the three target lesions (lattice degeneration, retinal breaks, and retinal detachment) were graded as referable. IBM Spss Statistics 23 was used for the data analysis in this study (IBM, Armonk, New York, USA).

Results

After reviewing 1500 original Optos images, 995 images from 637 participants (mean age: 52 years; 56.2% female) were

qualified to make up the tessellated dataset. Further filtering out 84 images for non-target peripheral retinal lesions and inconsistent assessment, 911 eligible images were used to develop the deep-learning system, among which 267 images had been identified with lattice degeneration, while 49 with retinal breaks, 44 with retinal detachment, and 609 with normal peripheral retina. Of all the eligible images, 60% (532 images) were randomly assigned to the training set, while 20% (190 images) to the validation set and 20% (189 images) to the testing set. More information on datasets is shown in Table 2.

A total of 6 models were trained when 2 preprocessing approaches were used to develop deep-learning models for 3 target lesions (lattice degeneration, retinal breaks, and retinal detachment). Figure 2 presents the corresponding receiver operating characteristic curves for each lesion. The AUC of original resizing preprocessing method was higher in retinal detachment and lattice degeneration, while the better preprocessing approach was cropping method in retinal breaks. With the optimal preprocessing approach, an AUC of 1.00 (95% CI, 1.00-1.00) was achieved for retinal detachment, while an AUC of 0.888 (95% CI, 0.843-0.933) and 0.953 (95% CI, 0.923-0.983) were for lattice degeneration and retinal breaks respectively. In addition, sensitivity and specificity at the highest harmonic mean for each lesion were measured and are presented in Table 3.

Tessellated fundus detected with any one of the lattice degeneration, retinal breaks, and retinal detachment should be referred to retinal specialists for further evaluation. The referral accuracy of our screening system based on the optimal deep-learning models was 79.8% compared to the reference standard.

All misclassified images were analyzed by category based on the corresponding optimal deep-learning model. For retinal detachment, 2 images presenting shallow retinal detachment were misclassified as normal (Fig. 3a), while none misclassified as retinal detachment.

For lattice degeneration, 6 lattice degeneration images were misclassified as normal all due to edge location of lesions (Fig. 3b), while 23 normal peripheral retina images misclassified as lattice degeneration. The most common characteristics of false-positive cases were vitreoretinal traction or proliferative vitreous membrane (87.0%, 20/23) (Fig. 4).

For retinal breaks, 2 retinal break images with lesions partly covered by upper eyelid were misclassified as normal (Fig. 3c), while 11 normal peripheral retina images misclassified as retinal breaks. The common characteristics of false-positive cases included vitreoretinal traction (n = 3), lattice degeneration (n = 2), eyelashes mimicking break edges (n = 2), and dark regions within detached retina surrounded by vitreoretinal traction folds (n = 2) (Fig. 5).

Discussion

In the pilot study, we developed a combined deep-learning system based on Optos images for the detection of lattice degeneration, retinal break, and retinal detachment in tessellated eyes. Three models with optimal preprocessing approaches were involved in the system, which showed remarkable performance for retinal detachment (AUC 1.000, sensitivity 0.875, and specificity 1.000) and moderate performance for retinal breaks (AUC 0.953, sensitivity 0.875, and specificity 0.924) and lattice degeneration (AUC 0.888, sensitivity 0.771, and specificity 0.797). The system offered a cost-effective way to distinguish the three most notable peripheral retinal lesions from normal in tessellated eyes at one

Table 2 Number of images in training, validation, and testing datasets with two image preprocessing methods

	Training set, no. (%)	Validation set, no (%)	Testing set, no. (%)
Origin			
Lattice degeneration	151 (28.4)	59 (31.1)	57 (30.2)
Retinal breaks	16 (3.0)	17 (8.9)	16 (8.5)
Retinal detachment	16 (3.0)	12 (6.3)	16 (8.5)
Normal peripheral retina	366 (68.8)	122 (64.2)	121 (64.0)
Total	532 (100)	190 (100)	189 (100)
Crop and augmentation			
Lattice degeneration	4500	1700	NA
Retinal breaks	340	500	NA
Retinal detachment	340	260	NA
Normal peripheral retina	23,047	22,240	NA
Total	28,227	24,700	NA

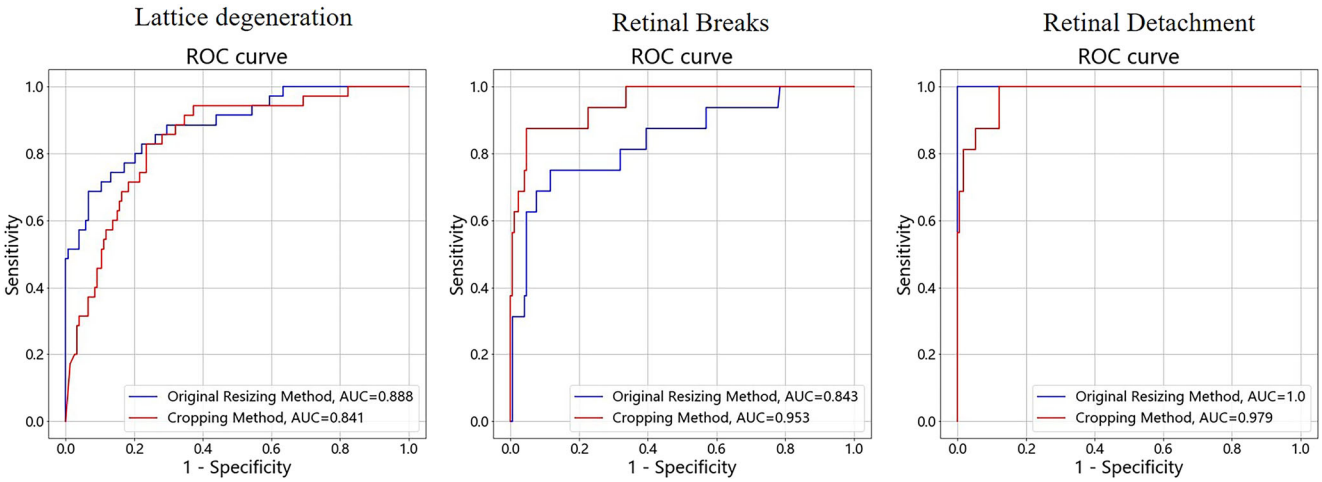

Fig. 2 Receiver operating characteristic (ROC) curves for lattice degeneration, retinal breaks, and retinal detachment

time, and the reasonable referral accuracy achieved by the system compared to the reference standard indicated it as a potential screening tool in primary care with low accessibility to retinal specialists. Moreover, it can be performed in patients who cannot tolerate pupil dilation. To the best of our knowledge, this study was the first to establish a deep-learning system for combined detection of lattice degeneration, retinal breaks, and retinal detachment in tessellated eyes based on Optos images (Fig. 6).

Deep-learning systems in identifying retinal detachment or notable peripheral retinal lesions (NPRL, including lattice degeneration and retinal breaks) on Optos images were reported with high accuracies in previous studies [10–12]. However, none of them could evaluate both retinal detachment and notable peripheral retinal lesions simultaneously, and lattice degeneration and retinal breaks were not further classified independently. For notable peripheral retinal lesions that have progressed to peripheral retinal detachment, urgent referrals and timely appropriate treatment are desperately required. Missing report of retinal detachment by NPRL-only screening system could pose significant risks to these subjects. Classification of NRPL is also necessary since management and follow-up are recommended mainly based on the presence of retinal breaks and their types according to PPP guidelines. Horseshoe tear, one of the retinal breaks, is in need of prompt referral and treatment, while lattice degeneration needs only monitoring in most cases [15]. Classifications in our system may implicate the varying degree of referral urgency.

The CNN seResNext50 used in our study has previously been shown to be effective in natural scene image classification. By this algorithm, 2 models with different preprocessing approaches were established for each target

Table 3 Performance of the deep-learning models in detection of for lattice degeneration, retinal breaks, and retinal detachment with two preprocessing methods

	AUC (95% CI)	Sensitivity (95% CI)	Specificity (95% CI)	Accuracy (95% CI)
Lattice degeneration				
Original resizing method	0.888 (0.843, 0.933)	0.771 (0.712,0.831)	0.797 (0.74,0.855)	0.793 (0.735,0.85)
Cropping method	0.841 (0.788, 0.893)	0.829 (0.775, 0.882)	0.752 (0.69, 0.813)	0.766 (0.706, 0.826)
Retinal breaks				
Original resizing method	0.843 (0.791, 0.895)	0.625 (0.556, 0.694)	0.953 (0.923, 0.984)	0.926 (0.888, 0.963)
Cropping method	0.953 (0.923, 0.983)	0.875 (0.828, 0.922)	0.924 (0.887, 0.962)	0.920 (0.882, 0.959)
Retinal detachment				
Original resizing method	1.00 (1.00, 1.00)	0.875 (0.828, 0.922)	1.00 (1.00, 1.00)	0.989 (0.975, 1.00)
Cropping method	0.979 (0.958, 0.999)	0.812 (0.757, 0.868)	0.953 (0.923, 0.984)	0.941 (0.908, 0.975)

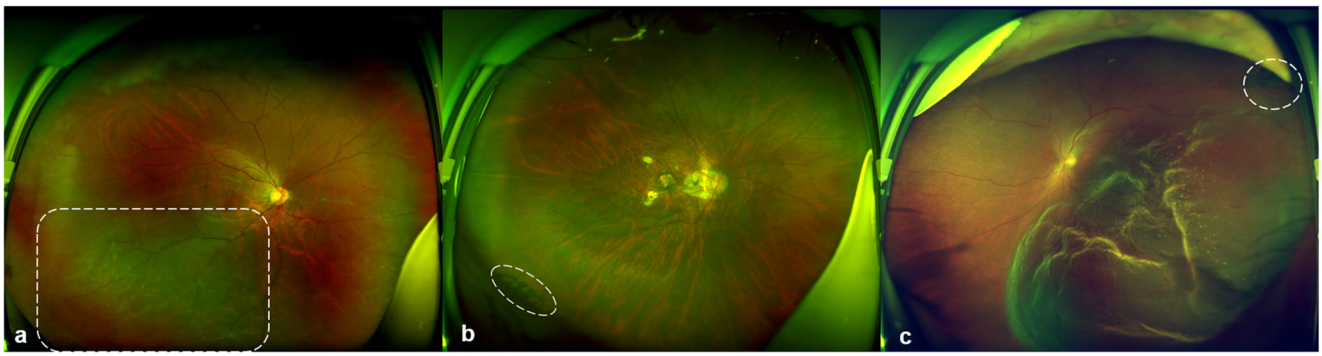

Fig. 3 Representative Optos images of false-negative cases. **a** Shallow retinal detachment in the inferotemporal quadrant (dashed rounded rectangle). **b** Lattice degeneration with pigmentation on the bottom left (dashed circle), partly covered by lower eyelid. **c** Retinal break on the top right (dashed circle), partly covered by the upper eyelid (true-positive for retinal detachment)

lesion. As shown in Fig. 2, the better preprocessing approach for retinal detachment and lattice degeneration is original resizing method, while cropping method achieved better outcome on retinal breaks. The difference may be explained by the lesion size. Lesions of retinal breaks are relatively small to ultra-wide-field images, for which cropping method enables the deep-learning system to learn more details about lesions. On the contrary, the range of retinal detachment and the size of lattice degeneration are often large enough for direct detection, and excessive irrelevant information may be augmented and interfere the training of deep-learning model.

In the study, we reviewed all the misclassified images by the optimal deep-learning system. For retinal detachment, both false-negative images were attributable to shallow retinal detachment. For lattice degeneration and retinal breaks, false-negative classification was due to peripheral location of lesions or eyelid covering, while the most common reason for false-positive cases was vitreoretinal traction in both groups. Pigmentary disturbances within lattice degeneration were misclassified as retinal breaks as shown by the heatmap in 2 false-positive images (Fig. 5b). The performance of our system may be improved by further training with more images of target lesions.

Our study has several limitations. First, as a pilot study, our system was developed on a relatively small dataset and was not validated by independent external dataset, which could be the main reason for the acceptable but not ideal performance of lattice degeneration and retinal break models, though preprocessing approaches had been optimized to improve the performance. Second, images with other peripheral retinal lesions rather than the 3 target ones were not assessed, and unclear images due to vitreous hemorrhage or intense cataracts were not included as well. We excluded postoperative eyes for regular follow-ups they should have with retinal specialists, in which our screening system was not indicated. Third, even though up to 200° of retina can be captured by Optos, some peripheral regions, especially superior and inferior peripheral areas hidden by eyelids and eyelashes, are still not covered. Pseudocolors and peripheral distortion of Optos images compromised the reliability of using consensus of specialists as reference standard. Goldmann three-mirror contact lens examination as adjudication

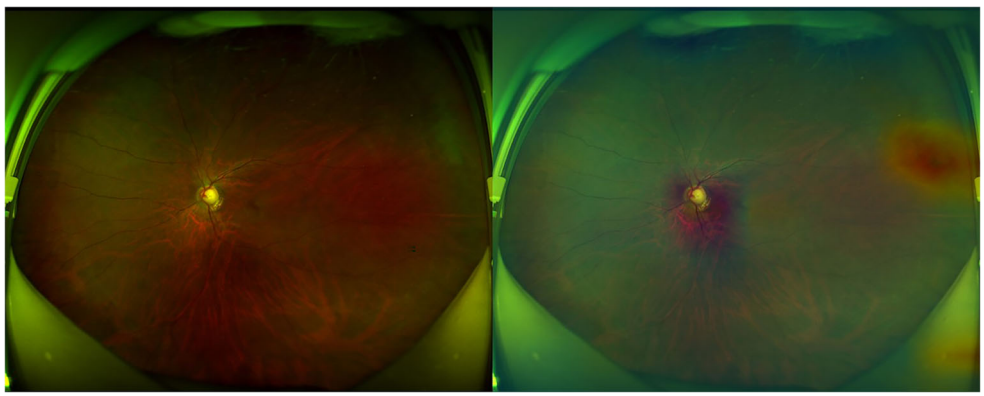

Fig. 4 Representative Optos image and corresponding heatmap of false-positive case for lattice degeneration. Peripheral vitreoretinal traction shown on the right of the Optos image displays red in the corresponding heatmap

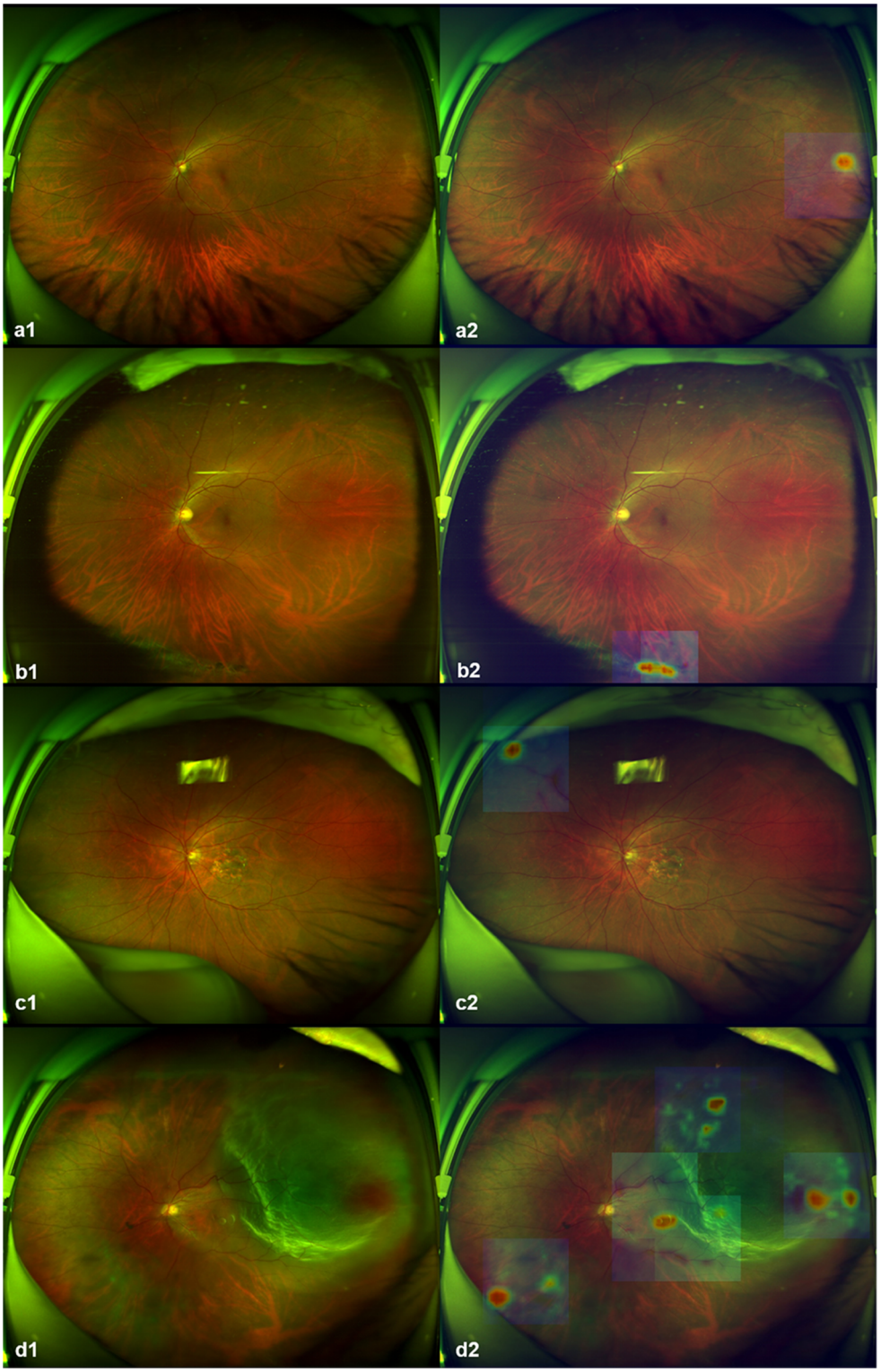

Fig. 5 Representative Optos images and corresponding heatmaps of false-positive cases for retinal breaks. **a** Vitreoretinal traction with punctate hemorrhage shown on the right of a1 presents red in heatmap a2. **b** Lattice degeneration shown on the bottom of b1 displays red in heatmap b2. **c** Eyelashes mimicking break edges shown on top left of c1 becomes red in heatmap c3. **d** Several relative dark regions within detached superotemporal retina shown in d1 manifests red in heatmap d2

process of determining peripheral retinal lesions would be combined for further validation of the algorithms in the future. Moreover, our deep-learning system was developed on selected tessellated eyes, and further studies with larger sample sizes are needed to validate the generalizability of this system for all eyes.

In summary, the study preliminarily verifies the feasibility of our deep-learning system as a screening tool to detect lattice

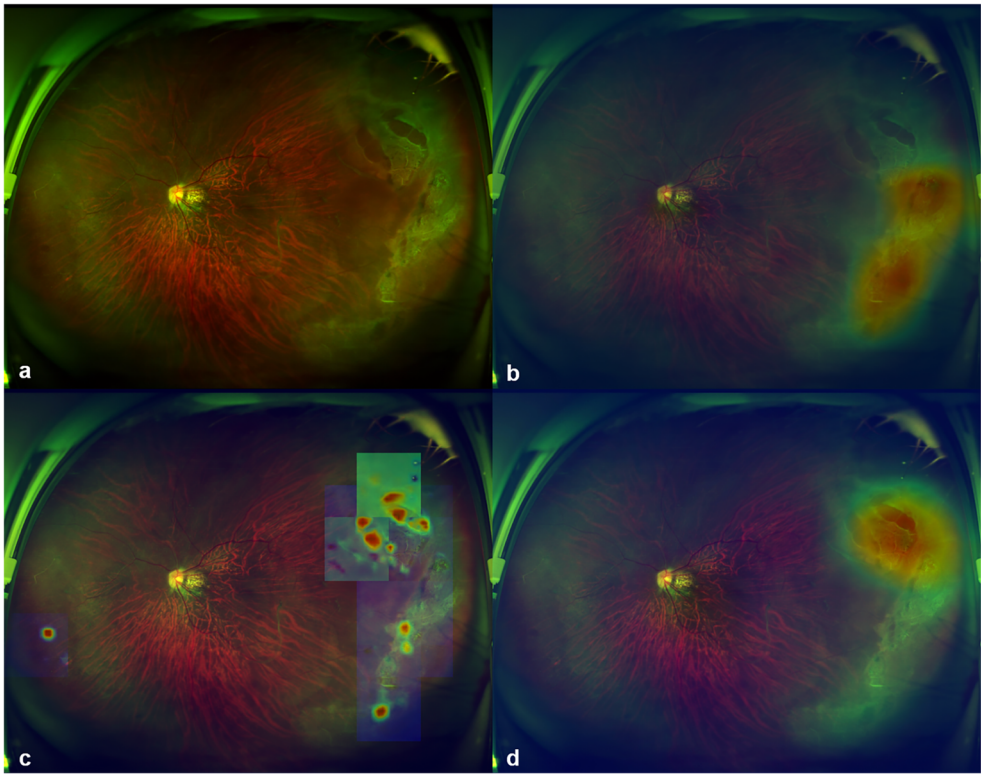

Fig. 6 Combined detection of lattice degeneration, retinal breaks, and retinal detachment in a true-positive case. The three target lesions shown in **a** are highlighted respectively in heatmap **b** (lattice degeneration), **c** (retinal breaks), and **d** (retinal detachment)

degeneration, retinal breaks, and retinal detachment in tessellated eyes using ultra-wide-field images. Future research is necessary to validate the algorithms with external datasets and investigate the feasibility of applying the system in clinical setting.

Author contribution CZ and FH proposed the idea and designed the study. CZ, FH, and BL assessed and annotated images. CZ wrote the original manuscript, while FH and BL revised it. CZ, FH, and BL contributed equally to this work. HW and XH were in charge of training the deep-learning system and participated in writing the corresponding section (the "Development of deep-learning system" section) in the "Methods" section of the manuscript under the guidance of XL. WY and YC helped with study design and revision of manuscripts, and the conduction of this study was supervised by them.

Funding This study was funded by Chinese Academy of Medical Sciences Initiative for Innovative Medicine (2018-I2M-AI 001), pharmaceutical collaborative innovation project of Beijing Science and Technology Commission (Z191100007719002), National Natural Science Foundation of China (NSFC) (61672523), and Beijing Natural Science Foundation (4202033).

Availability of data and material Data are available on reasonable request.

Code availability Not applicable.

Declarations

Ethics approval This retrospective study was in accordance with the ethical standards of Peking Union Medical College Hospital Institutional Review Board (No. S-K631) and with the 1964 Helsinki declaration and its later amendments or comparable ethical standards.

Informed consent Informed consent was granted exemption since all images were deidentified.

Consent for publication Not applicable.

Consent to participate Not applicable.

Conflict of interest The authors declare no competing interests.

References

1. Holden BA, Fricke TR, Wilson DA et al (2016) Global prevalence of myopia and high myopia and temporal trends from 2000 through 2050. Ophthalmology 123(5):1036–1042
2. Ohno-Matsui K, Lai TY, Lai CC, Cheung CM (2016) Updates of pathologic myopia. Prog Retin Eye Res 52:156–187
3. Mitry D, Singh J, Yorston D et al (2011) The predisposing pathology and clinical characteristics in the Scottish retinal detachment study. Ophthalmology 118(7):1429–1434
4. Wilkinson CP (2000) Evidence-based analysis of prophylactic treatment of asymptomatic retinal breaks and lattice degeneration. Ophthalmology 107(1):12–15 discussion 15-18
5. Mitry D, Charteris DG, Fleck BW et al (2010) The epidemiology of rhegmatogenous retinal detachment: geographical variation and clinical associations. Br J Ophthalmol 94(6):678–684
6. Jagadeesh D, Philip K, Naduvilath TJ et al (2019) Tessellated fundus appearance and its association with myopic refractive error. Clin Exp Optom 102(4):378–384. https://doi.org/10.1111/cxo.12822

7. Koh VT, Nah GK, Chang L et al (2013) Pathologic changes in highly myopic eyes of young males in Singapore. Ann Acad Med Singap 42(5):216–224
8. Witmer MT, Parlitisis G, Patel S et al (2013) Comparison of ultra-widefield fluorescein angiography with the Heidelberg Spectralis(®) noncontact ultra-widefield module versus the Optos(®) Optomap(®). Clin Ophthalmol 7:389–394
9. Nagiel A, Lalane RA, Sadda SR, Schwartz SD (2016) Ultra-widefield fundus imaging: a review of clinical applications and future trends. Retina 36(4):660–678
10. Ohsugi H, Tabuchi H, Enno H, Ishitobi N (2017) Accuracy of deep learning, a machine-learning technology, using ultra-wide-field fundus ophthalmoscopy for detecting rhegmatogenous retinal detachment. Sci Rep 7(1):9425
11. Li Z, Guo C, Nie D et al (2019) A deep learning system for identifying lattice degeneration and retinal breaks using ultra-widefield fundus images. Ann Transl Med 7(22):618
12. Li Z, Guo C, Nie D et al (2020) Deep learning for detecting retinal detachment and discerning macular status using ultra-widefield fundus images. Commun Biol 3(1):15
13. Matsuba S, Tabuchi H, Ohsugi H et al (2019) Accuracy of ultra-wide-field fundus ophthalmoscopy-assisted deep learning, a machine-learning technology, for detecting age-related macular degeneration. Int Ophthalmol 39(6):1269–1275
14. Nagasawa T, Tabuchi H, Masumoto H et al (2018) Accuracy of deep learning, a machine learning technology, using ultra-wide-field fundus ophthalmoscopy for detecting idiopathic macular holes. PeerJ 6:e5696
15. Flaxel CJ, Adelman RA, Bailey ST et al (2020) Posterior Vitreous Detachment, Retinal Breaks, and Lattice Degeneration Preferred Practice Pattern®. Ophthalmology 127(1):P146–P181
16. Hu J, Shen L, Albanie S et al (2019) Squeeze-and-excitation networks. IEEE Trans Pattern Anal Mach Intell. https://doi.org/10.1109/tpami.2019.2913372
17. Xie S, Girschick R, Dollár P et al (2017) Aggregated residual transformations for deep neural networks. IEEE Conf Comput Vis Pattern Recognit 2017:5987–5995. https://doi.org/10.1109/CVPR.2017.634
18. Zhou B, Khosla A, Lapedriza A et al (2016) Learning deep features for discriminative localization. IEEE Conf Comput Vis Pattern Recognit 2016:2921–2929. https://doi.org/10.1109/CVPR.2016.319